Local shear stress and its correlation with local volume fraction in concentrated non-Brownian suspensions: Lattice Boltzmann simulation

Young Ki Lee, Kyung Hyun Ahn,* and Seung Jong Lee
School of Chemical and Biological Engineering, Institute of Chemical Process, Seoul National University, Seoul, 151-744 Korea
(Received 1 July 2014; revised manuscript received 19 October 2014; published 29 December 2014)

The local shear stress of non-Brownian suspensions was investigated using the lattice Boltzmann method coupled with the smoothed profile method. Previous studies have only focused on the bulk rheology of complex fluids because the local rheology of complex fluids was not accessible due to technical limitations. In this study, the local shear stress of two-dimensional solid particle suspensions in Couette flow was investigated with the method of planes to correlate non-Newtonian fluid behavior with the structural evolution of concentrated particle suspensions. Shear thickening was successfully captured for highly concentrated suspensions at high particle Reynolds number, and both the local rheology and local structure of the suspensions were analyzed. It was also found that the linear correlation between the local particle stress and local particle volume fraction was dramatically reduced during shear thickening. These results clearly show how the change in local structure of suspensions influences the local and bulk rheology of the suspensions.

DOI: 10.1103/PhysRevE.90.062317 PACS number(s): 83.10.Rs

I. INTRODUCTION

Understanding the rheology of particle suspensions is important in designing the materials and processes of many industrial applications such as electronic materials and secondary batteries to name a few, and many studies are still done to understand the complex flow behaviors of these complex fluids [1]. One of the key issues in suspension rheology is the shear thickening behavior which is often observed in hard-sphere suspensions, especially, at high volume fraction. Shear thickening of hard-sphere suspensions has been widely studied in experiments [2–6]. Structural evolution of particle suspensions during shear thickening was probed by rheo-optical experiments [4] and by small angle neutron scattering (SANS) [5]. Recently, the internal structure of a suspension in both shear thinning and shear thickening was directly observed by fast confocal microscopy [6]. However, despite the progress of experimental techniques, direct observation of the microstructure still has many limitations. Therefore, numerical simulation needs to be done to support experimental observations and to theoretically explain the various phenomena of these complex fluids. One representative numerical study for hard-sphere suspensions was performed by Brady and co-workers using the Stokesian dynamics (SD) [7–9] and accelerated Stokesian dynamics (ASD) simulation techniques [10]. SD has been widely used because it considers many-body hydrodynamic interactions accurately at the low Reynolds number region. Foss and Brady [9] investigated the nonequilibrium behavior of concentrated Brownian suspensions under a simple shear flow. They focused on the effect of the Péclet number on the particle dynamics, and shear thickening at the high Péclet number region (hydrodynamic dominant region) was successfully captured. In that study, they showed that the lubrication force has a crucial role in forming clusters among the approaching particles, and these clusters can trigger shear thickening in hard-sphere suspensions. They also explained how anisotropy in the pair-distribution function affects the rheology of the suspensions. In this way, the SD algorithm contributed to understanding suspension rheology including shear thickening, but it also has several limitations. One is that only the flow behavior can be explained at low Reynolds number; that is to say, only a system in which the inertia effect is negligible can be considered. In real processes, suspensions that include various sizes of particles from several nanometers to several millimeters are commonly used. Furthermore, they are usually transported under complex flow situations at a high flow rate. In these conditions, the inertia may not be negligible. Therefore, understanding flow behavior with inertia is quite important. Taking inertia into consideration at finite Reynolds number is still challenging. Though a study on particle suspensions with inertia has been carried out by direct numerical simulation (DNS) [11], only a few studies have been done due to high computational cost. Recently, the lattice Boltzmann method (LBM) has been introduced, and it has been widely applied to investigate various fluid dynamics problems [12] as well as the dynamics of particle suspensions [13] at finite Reynolds number. Shakib-Manesh *et al.* [14] successfully predicted the relative shear viscosity of non-Brownian suspensions in a two-dimensional (2D) Couette flow by LBM, and they reported on the shear thickening behavior of hard-sphere suspensions at high particle Reynolds number. Raiskinmäki *et al.* [15] captured shear thickening, and they tried to correlate shear thickening with particle clustering in a regime where hydrodynamic forces are dominant. Kromkamp *et al.* [16] also studied non-Brownian suspensions by LBM, and they compared the flow behaviors of 2D and three-dimensional (3D) suspensions in a laminar flow. They investigated the shear viscosity of the suspensions and reasonable results were confirmed in both cases. Kulkarni and Morris [17] reported the rheology of 3D particle suspensions at finite Reynolds number, and successfully observed an increase in the shear stress as well as in the normal stress with an increase in inertia. Although there have been many studies on the non-Newtonian behavior of suspensions, only wall shear stress or bulk shear stress [18] has been measured in simulations. They have limitations in investigating local shear stress, and it is hard to explain how local structural evolution affects the rheology

*Corresponding author: ahnnet@snu.ac.kr

in a local region and subsequently, the bulk rheology of suspensions.

Therefore, this study investigated the "local rheology" of non-Brownian suspensions with a readopted algorithm. For non-Brownian suspensions, wall shear stress and local shear stress were measured for various particle volume fractions, and they were correlated with locally evolved particle microstructures. To describe non-Brownian suspensions, smoothed profile method (SPM) [19], which was successfully coupled with LBM, was adopted, and the method of planes (MOP) [20] was additionally applied to access the local stress of the suspensions. The paper is organized as follows. Numerical methods and the computational algorithm are introduced in Sec. II, and the simulation results are provided in Sec. III. The simulation conditions with algorithm verification are explained in Secs. III A and III B, and the shear viscosity of the suspension is reported in Sec. III C. In Sec. III D, the shear thickening behavior of a concentrated suspension is discussed, and the microstructure of the suspension is analyzed to find the origin of shear thickening in Sec. III E. Furthermore, the local rheology and its correlation with the microstructure are explained in Sec. III F, and finally, conclusions are given in Sec. IV.

II. NUMERICAL METHOD

A. Lattice Boltzmann method (LBM)

Since its introduction two decades ago, the lattice Boltzmann method (LBM) has been recognized as a useful tool in computational fluid dynamics, and it has been widely adopted for various applications such as microfluidics, turbulent flows, and multiphase systems due to its easy implementation [12]. In LBM, macroscopic dynamics can be described by the lattice Boltzmann equation (LBE) which is an approximate and discretized form of the Boltzmann equation. While conventional methods such as the finite element method (FEM) or finite volume method (FVM) directly solve Navier-Stokes (NS) equations, the LBM introduces virtual particles which are the packets of mesoscopic particles [12,13]. The evolution of the probability distribution function is given by the lattice Boltzmann equation with the Bhatnagar-Gross-Krook (BGK) collision operator [21] which takes the form of Eq. (1). By solving this equation, the incompressible Navier-Stokes (NS) equations can be correctly recovered [21].

$$f_i(\mathbf{x}+\mathbf{c}_i\Delta t, t+\Delta t) - f_i(\mathbf{x},t) = -\frac{1}{\tau}\left[f_i(\mathbf{x},t) - f_i^{\mathrm{eq}}(\mathbf{x},t)\right]. \tag{1}$$

The LBM algorithm consists of streaming and collision steps. At the streaming step, the probability distribution function from the previous time step is propagated along the discretized velocity vector $\mathbf{c}_i$ to the next neighbor lattice nodes. This process can be imposed by the left-hand side of Eq. (1), where $\mathbf{x}$ is the position of the lattice node at time t; $\mathbf{c}$ is the discrete velocity, and f_i is the distribution function for the i direction. τ denotes the dimensionless relaxation time of the solvent, and it is related to the kinematic viscosity, $\nu = c_s^2(\tau - 1/2)\Delta x^2/\Delta t$ [21]. In our study, the D2Q9 lattice model was used which was designed to consider nine direction velocities in two-dimensional space [12]. The speed of sound has the form of $c_s = \sqrt{1/3}\Delta x/\Delta t$, where Δx and Δt denote the lattice spacing and time step, respectively. After the streaming step, the probability distribution function is determined for each lattice point with the collision step, according to the right-hand side of Eq. (1). During this process, momentum conservation is constrained by the equilibrium distribution, f_i^{eq}, which is determined by Eq. (2).

$$f_i^{\mathrm{eq}}(\mathbf{x}) = w_i\rho\left[1 + \frac{\mathbf{c}_i\cdot\mathbf{u}}{c_s^2} + \frac{(\mathbf{c}_i\cdot\mathbf{u})^2}{2c_s^4} - \frac{\mathbf{u}\cdot\mathbf{u}}{2c_s^2}\right]. \tag{2}$$

The equilibrium distribution can be obtained by the truncated form of the Maxwell distribution, and it is well known as a good approximation for small Mach numbers [21]. The macroscopic properties of the solvent such as the density ρ and the velocity $\mathbf{u}$ are obtained from the zeroth and first velocity moments of the distribution function f_i shown in Eqs. (3) and (4).

$$\rho = \sum_i f_i, \tag{3}$$

$$\rho\mathbf{u} = \sum_i f_i\mathbf{c}_i. \tag{4}$$

Direction dependent weight coefficients w_i and the lattice velocity $\mathbf{c}_i$ were used according to Table I.

B. Smoothed profile method (SPM)

Various algorithms have been suggested to consider the motion of solid particles in LBM [22–26], and they have been widely used to investigate the dynamics and rheology of suspensions [14–17]. In this study, the smoothed profile method (SPM) was adopted, which has been successfully combined with LBM [19]. SPM is a promising numerical algorithm, which considers multibody hydrodynamic interactions among solid particles accurately and efficiently, and has been successfully applied to a neutrally buoyant cylinder under simple shear flow, sedimentation of two circular cylinders, and so on [19,27–29]. In SPM, the boundaries between solid objects and the host solvent are replaced with a continuous interface by assuming a smoothed profile, so that the discontinuity problem, which arises on the boundary of solid objects, can be dramatically reduced. SPM is also efficient because it does not need additional Lagrangian nodes [27] near the surface of solid objects. Furthermore, it is more accurate for momentum

TABLE I. Weight coefficients w_i and the lattice velocity $\mathbf{c}_i$ in D2Q9 lattice model.

	$i=0$	$i=1$	$i=2$	$i=3$	$i=4$	$i=5$	$i=6$	$i=7$	$i=8$
w_i	4/9	1/9	1/9	1/9	1/9	1/36	1/36	1/36	1/36
$\mathbf{c}_i$	(0,0)	(1,0)	(0,1)	(−1,0)	(0, −1)	(1,1)	(−1,1)	(−1, −1)	(1, −1)

conservation than that of other link-based methods [22–24]. In SPM, the profile function $\phi_P(\mathbf{x})$ that defines a spherical particle (cylinder in 2D) can be chosen arbitrarily, but in this study, it was defined in the form of Eq. (5) as follows:

$$\phi_P(\mathbf{x}) = \frac{1}{2}\left[1 + \tanh\frac{R - |\mathbf{x} - \mathbf{X}|}{\xi}\right]. \tag{5}$$

Here, R is the radius of the solid particle; $\mathbf{X}$ is the center position of the solid particle, and $\mathbf{x}$ is the position of the lattice node. In the fluid region, $\phi_P = 0$ while $\phi_P = 1$ in the solid particle region, and its value changes continuously at the interfacial region. The interface thicknesses was controlled by parameter ξ, and the accuracy can be enhanced by controlling ξ [19,27]. In this study, $\xi = 1$ was applied which is commonly used in the literature, and the cutoff radius was set as $R_{\text{cutoff}} = R + \Delta x$ for an efficient calculation.

The solvent-solid interaction force on solid boundary node, $\mathbf{x}$ at time t, can be evaluated by Eq. (6) with the assumption that the forces and torque are distributed during the interval time Δt as follows:

$$\mathbf{f}_P(\mathbf{x},\mathrm{t}) = \phi_P(\mathbf{x},t)\left[\mathbf{u}_P(\mathbf{x},t) - \mathbf{u}(\mathbf{x},t)\right]/\Delta t, \tag{6}$$

where $\mathbf{u}$ is the macroscopic velocity at the solvent node which was defined in Eq. (4), and $\mathbf{u}_P$ is the velocity at the solid node. $\mathbf{u}_P$ is defined in terms of the translation velocity of the solid particle $\mathbf{U}$ and the angular velocity of the solid particle $\mathbf{\Omega}$ at the lattice node $\mathbf{x}$ covered by solid particles.

$$\mathbf{u}_P(\mathbf{x},t) = \mathbf{U} + \mathbf{\Omega} \times (\mathbf{x} - \mathbf{X}). \tag{7}$$

The hydrodynamic force affected by the solid particles to the solvent boundary node is calculated by Eq. (8);

$$\mathbf{f}_H(\mathbf{x},t) = -\mathbf{f}_P(\mathbf{x},\mathrm{t}), \tag{8}$$

and then, the hydrodynamic force $\mathbf{f}_H$ is added to the collision operator in Eq. (1) as a body force which considers the interaction between two phases. This process is presented by Eq. (9).

$$f_i(\mathbf{x} + \mathbf{c}_i\Delta t, t + \Delta t) - f_i(\mathbf{x},t) = -\frac{1}{\tau}\left[f_i(\mathbf{x},t) - f_i^{\text{eq}}(\mathbf{x},t)\right] + \frac{w_i\Delta t}{c_s^2}[\mathbf{f}_H(\mathbf{x},t)\cdot\mathbf{c}_i]. \tag{9}$$

The hydrodynamic force $\mathbf{F}_H$ and torque $\mathbf{T}_H$, which influence each particle, are calculated by Eqs. (10) and (11), respectively.

$$\mathbf{F}_H = \sum_{\mathbf{x}\in V_p} \rho(\mathbf{x})\mathbf{f}_P(\mathbf{x},\mathrm{t}), \tag{10}$$

$$\mathbf{T}_H = \sum_{\mathbf{x}\in V_p} (\mathbf{x} - \mathbf{x_s}) \times \rho(\mathbf{x})\mathbf{f}_P(\mathbf{x},\mathrm{t}). \tag{11}$$

Translation velocity and angular velocity of the solid particles at a new time step are obtained by Eqs. (12) and (13).

$$\mathbf{V}(t + \Delta t) = \mathbf{V}(t) + \frac{\mathbf{F}_H}{M_P}\Delta t, \tag{12}$$

$$\mathbf{\Omega}(t + \Delta t) = \mathbf{\Omega}(t) + \frac{\mathbf{T}_H}{I_P}\Delta t. \tag{13}$$

The mass of a solid particle M_P and the moment of inertia I_P are defined by Eq. (14) and Eq. (15), where ρ_P denotes the density of a solid particle.

$$M_P = \rho_P\pi R^2, \tag{14}$$

$$I_P = 0.5 M_P R^2. \tag{15}$$

The particle position is updated from the new particle velocity, which was obtained by Eq. (12), and it was integrated by the Adams-Bashforth method [30], as in Eq. (16), which has a second-order accuracy.

$$\mathbf{X}(t + \Delta t) = \mathbf{X}(t) + \left[\tfrac{3}{2}\mathbf{V}(t + \Delta t) - \tfrac{1}{2}\mathbf{V}(t)\right]\Delta t. \tag{16}$$

To prevent overlap among solid particles, the short range repulsive potential in Eq. (17) was additionally imposed. The potential has the form of the Weeks, Chandler, and Andersen (WCA) which has been widely used to describe nearly hard spheres [31]. σ is the diameter of a solid particle, r is the particle to particle center distance, and ε is the potential strength. In this work, ε was set to 0.1, and it was determined by trial and error not to allow overlap between the particles at the highest shear rate we could cover.

$$U_{PP}(r) = \begin{cases} \varepsilon\left[\left(\frac{\sigma}{r}\right)^{36} - \left(\frac{\sigma}{r}\right)^{18}\right], & r \leqslant 2^{1/18}\sigma, \\ 0, & r > 2^{1/18}\sigma. \end{cases} \tag{17}$$

When two particles come into close contact with each other, the lubrication force becomes important. However, the lubrication force cannot be exactly resolved with LBM when the gap distance between two particles is on the order of one lattice spacing due to the discretization of the particles and fluids. To overcome this problem, a lubrication correction method based on an explicit calculation of the lubrication force was introduced [16,23]. For a 3D system, it is given by

$$\mathbf{F}_{\text{lub}} = \begin{cases} -6\pi\eta\frac{a_1^2a_2^2}{(a_1+a_2)^2}\left(\frac{1}{h} - \frac{1}{h_c}\right)\mathbf{U}_{12}\cdot\hat{\mathbf{R}}_{12}, & h < h_c, \\ 0, & h > h_c. \end{cases} \tag{18}$$

Here, a_1 and a_2 denote the radius of two solid particles, and they have the same value a in the monodisperse system. η means the solvent viscosity; $\mathbf{U}_{12} = \mathbf{U}_1 - \mathbf{U}_2$ denotes the relative velocity of the particles, and $\hat{\mathbf{R}}_{12} = (\mathbf{R}_1 - \mathbf{R}_2)/|\mathbf{R}_1 - \mathbf{R}_2|$ is a unit vector between two particles. h is the surface to surface distance of two particles and h_c is the cutoff distance.

The analytically derived equation by Kromkamp *et al.* [16] was adopted for a 2D particle (cylinder), which is defined as follows.

$$\mathbf{F}_{\text{lub}} = \begin{cases} -\frac{1}{2}\eta\mathbf{U}_{12}\cdot\hat{\mathbf{R}}_{12}\hat{\mathbf{R}}_{12}\left[\left(\frac{a_1+a_2}{h}\right)^{3/2}\left(F_0 + \frac{h}{a_1+a_2}F_1\right) - \left(\frac{a_1+a_2}{h_c}\right)^{3/2}\left(F_0 + \frac{h_c}{a_1+a_2}F_1\right)\right], & h < h_c, \\ 0, & h > h_c. \end{cases} \tag{19}$$

$h_c = 1.5\Delta x$ was adopted, and it was determined by the lubrication test for two approaching particles (it will be discussed in the next section). Even though this value is a little different from the optimum cutoff distance used by Kromkamp *et al.* [16] ($1.1\Delta x$ for a 3D system and $2.0\Delta x$ for a 2D system), the verification test confirms that $h_c = 1.5\Delta x$ is also reasonable in this system. F_0 is the numerical constant, and F_1 is the first-order correction to the lubrication limit, $h/2a \ll 1$. In this study, they were determined as $\frac{3}{4}\pi\sqrt{2}$ and $\frac{231}{80}\pi\sqrt{2}$, respectively, from the analytical derivation by Kromkamp *et al.* [16].

C. Moving wall boundary condition

To apply shear flow in a confined system, the halfway bounce-back method [22,23] was imposed, which is commonly used to describe the no-slip or moving wall boundary condition in LBM. In this algorithm, fluid distribution hitting a solid wall during propagation is bounced back in the direction it came from, and this microscopic boundary rule finally leads to a no-slip behavior of the macroscopic fluids at the wall. To describe the moving wall with velocity $\mathbf{u}_\mathrm{w}$, the original equation is modified as in Eq. (20), where f_i^* means the fluid distribution after the collision process, and i' denotes the inverse direction of i. The newly added term in the right-hand side of Eq. (20) captures the additional momentum transfer by the motion of the wall.

$$f_{i'}(\mathbf{x}, t+\Delta t) = f_i^*(\mathbf{x},t) - \frac{2w_i\rho(\mathbf{x},t)\mathbf{u}_\mathrm{w}\cdot\mathbf{c}_i}{c_s^2}. \tag{20}$$

During the bounce-back process, the wall momentum exchange Δp can be derived by Eq. (21),

$$\Delta p_{i'}\left(\mathbf{x}_w, t+\frac{1}{2}\Delta t\right) = \left[2f_i^*(\mathbf{x},t) - \frac{2w_i\rho(\mathbf{x},t)\mathbf{u}_\mathrm{w}\cdot\mathbf{c}_i}{c_s^2}\right]\mathbf{c}_i. \tag{21}$$

It is straightforward to evaluate the wall shear stress through the wall momentum exchange Δp per time Δt. It can be obtained by Eq. (22), where A is the wall surface area (the length of the wall boundary in a 2D case),

$$\sigma^w = \frac{\Delta p_{i'}}{\Delta t A}. \tag{22}$$

D. Shear stress measurement by the method of planes (MOP)

Measuring rheological properties from wall shear stress (WSS) is realistic and commonly accepted in rheometry. However, it does not allow the separation of solvent and particle contributions from the total stress, and the local shear stress of the fluid cannot be easily accessed. If the system is nonhomogeneous, it is more desirable to evaluate the local contribution of the solvent and particle to the total stress. However, it is hardly accessible in numerical simulations. To overcome this problem, a novel algorithm, the so-called method of planes (MOP), was proposed by Todd *et al.* [32]. This algorithm has successfully predicted the local stress of a simple liquid, and has been further applied to polymer melts [33]. Recently, it was extended to LBM coupled with the immersed boundary method (IBM) [20]. In this study, we applied the MOP algorithm to the smoothed profile method (SPM) with a slight modification. Even in this case, the solvent and particle contributions to total stress can be locally measured at each of the planes along the shear-gradient direction in the same manner as the original algorithm [20].

The solvent shear stress in each lattice node $\mathbf{x}$ at time t can be obtained by Eq. (23) [34,35], and the local solvent stress at plane Y was defined as Eq. (24), where j means the lattice nodes in plane Y.

$$\sigma_{xy}^s(\mathbf{x},t) = \left(1-\frac{\tau}{2}\right)\sum_i \left(f_i(\mathbf{x}) - f_i^{\mathrm{eq}}(\mathbf{x})\right)c_{xi}c_{yi}, \tag{23}$$

$$\sigma_{xy,\mathrm{local}}^s(Y,t) = \frac{1}{A}\sum_j \sigma_{xy}^s(j,t). \tag{24}$$

Imaginary plane y between lattice planes Y and $Y+\Delta Y$ (usually, $\Delta Y = 1$ in LBM) is assumed to calculate the local particle stress, and local particle stress at plane y is obtained by Eq. (25). In Krüger's work [20], $F_{jx}(t)$ was defined as the x component of the force imposed on the lattice node j at time t, and it could be directly measured by the interfacial tension or the membrane forces on the Lagrangian nodes (for soft particles). In the present SPM system, F_{jx} can be alternatively changed to the x component of the hydrodynamic force $\mathbf{f}_H$ on a solid particle in Eq. (9), and is considered at the lattice nodes covered with solid particles. The sign function, $\mathrm{sgn}(x)$ has the values of $+1$ or -1 depending on the sign of x, and A denotes the length of the domain size in the x direction (flow direction in our system) in the case of a 2D simulation. Local particle stress at lattice node Y can be obtained by the average of two planes separated by one lattice constant ΔY; it is given by Eq. (26). Finally, the total stress in plane Y can be locally evaluated by the sum of each stress component as shown in Eq. (27).

$$\sigma_{xy,\mathrm{local}}^p(y,t) = \frac{1}{2A}\sum_j F_{jx}(t)\mathrm{sgn}(y-Y), \tag{25}$$

$$\sigma_{xy,\mathrm{local}}^p(Y,t) = \frac{1}{2}\left[\sigma_{xy,\mathrm{local}}^p\left(Y+\frac{\Delta Y}{2},t\right) + \sigma_{xy,\mathrm{local}}^p\left(Y-\frac{\Delta Y}{2},t\right)\right], \tag{26}$$

$$\sigma_{xy,\mathrm{local}}^{tot}(Y,t) = \sigma_{xy,\mathrm{local}}^s(Y,t) + \sigma_{xy,\mathrm{local}}^p(Y,t). \tag{27}$$

To verify the MOP algorithm in LBM coupled with SPM, a preliminary test was performed as follows. The shear stress of a single particle placed at the center of a confined channel was measured by both WSS and MOP. The simulation domain was 100×102 (including wall nodes), and the solid particle diameter was set as $D = 20$. The dimensionless relaxation parameter τ was set to unity, and the kinematic viscosity was set as $\nu = 1/6$. The moving wall boundary condition in Eq. (20) was imposed for the upper and lower wall with a shear rate of $\dot{\gamma} = 10^{-4}$, and the periodic boundary condition was applied to the flow direction. As shown in Fig. 1(a), a shear stress developed in the simulation domain, and high stress was generated around a particle. The stress distribution for both the solvent and particle was measured by MOP, and it was plotted in terms of channel height H shown in Fig. 1(b) together with the result of the WSS. At the center of

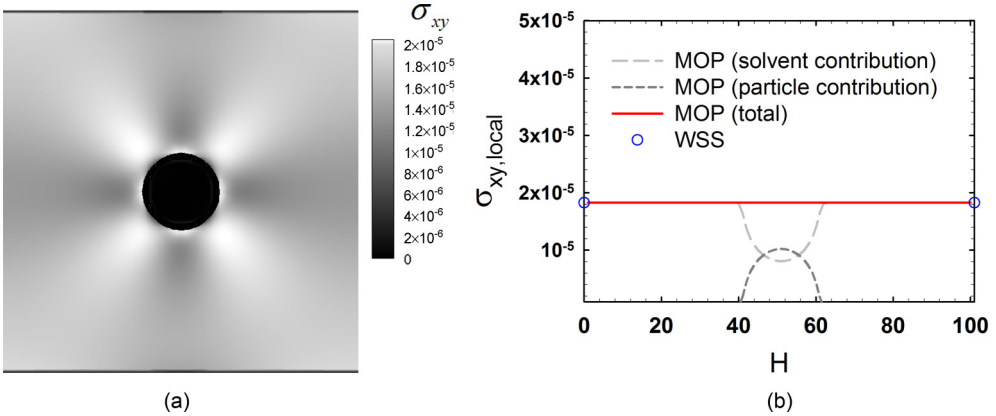

FIG. 1. (Color online) (a) Distribution of shear stress around a single particle and (b) stress distribution as a function of channel height, H.

the channel where the single particle was located, the stress contribution by the particle phase was dominant, and the total stress coincided well with that of the WSS. As verified by this result, the stress contribution from both the solvent and particle was well decomposed, and the local stress could be measured successfully in the present LBM coupled with SPM and MOP.

III. RESULTS AND DISCUSSION

A. Simulation setup

In this study, LBM was adopted as a solvent solver, and SPM was coupled with LBM to describe the motion of particles that had a hydrodynamic interaction. A solvent density of $\rho = 1$, dimensionless relaxation time of $\tau = 0.8$, and kinematic viscosity of $\nu = 0.1$ were used. For solid particles, a non-Brownian particle was assumed, and the particle diameter and particle density were set to $D = 20$ and $\rho_p = 1$. These material properties correspond to a real solvent system with a density of 1000 kg/m^3, kinematic viscosity of $\nu = 10^{-6}$m^2/s, and to real hard-sphere particles with a diameter of 20 μm and a density of 1000 kg/m^3. In this case, the lattice unit length and unit time are $\Delta x = 1$ μm and $\Delta t = 0.1$ μs, respectively. The simulations were performed for suspensions with the following particle volume fractions and numbers of solid particles: $\phi =$ 0.1, 0.2, 0.3, 0.4, 0.5, and 0.6; and 49, 100, 156, 204, 255, and 306, respectively. The size of the simulation domain was 400 × 402 (width × height, including wall nodes), and the channel height was 400, which corresponds to 400 μm in a real system. It is large enough compared to the particle diameter of 20 μm, and it is quite similar to the usual gap size of 500–1000 μm in the rotational rheometer in real experiments. Moving wall boundary conditions were imposed to both the upper and lower walls, and the periodic boundary condition was used in the flow direction.

B. Algorithm verification

To confirm the wall effect, the rotation of a single particle in a Couette flow was investigated for varying ratios of channel height to particle radius, H/R. The angular velocity of the particle at the centerline was calculated. The solvent density and the kinematic viscosity were set to $\rho = 1$ and $\nu = 0.1$. For solid particles, the diameter was $D = 20\,(R = 10)$, and the density was $\rho_p = 1$. The height of the channel H was 25–300, and the size of the simulation domaion was $400 \times (H + 2)$. For the upper and lower walls, the wall boundary condition was imposed at a shear rate of $\dot{\gamma} = 5 \times 10^{-6}$. In Fig. 2, the equlibrium angular velocity of a particle ω is plotted as a normalized one which was divided by the shear rate at the wall. When the ratio of the channel height to particle radius H/R is low, the normalized ω was less than 0.5 due to the strong influence of the wall. As the channel height is increased, the flow disturbance by the wall is reduced, and the normalized

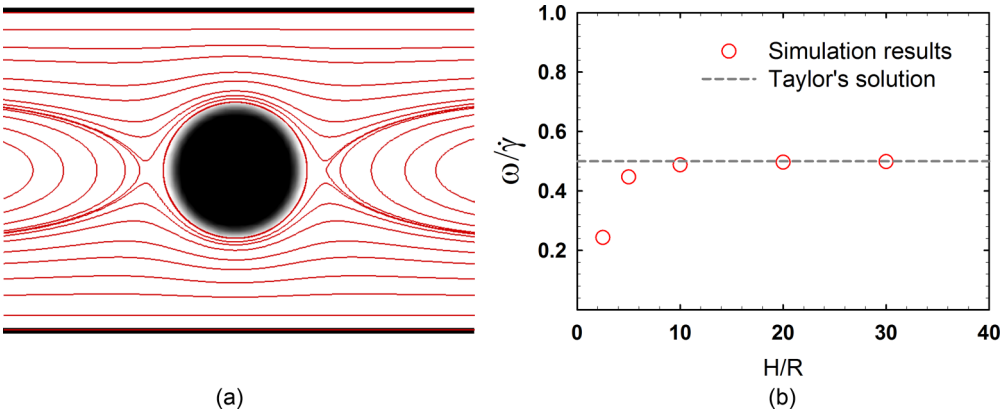

FIG. 2. (Color online) (a) Streamlines around a single particle in Couette flow for $H/R = 5$. (b) Normalized angular velocity for different ratio of channel height to particle radius, H/R.

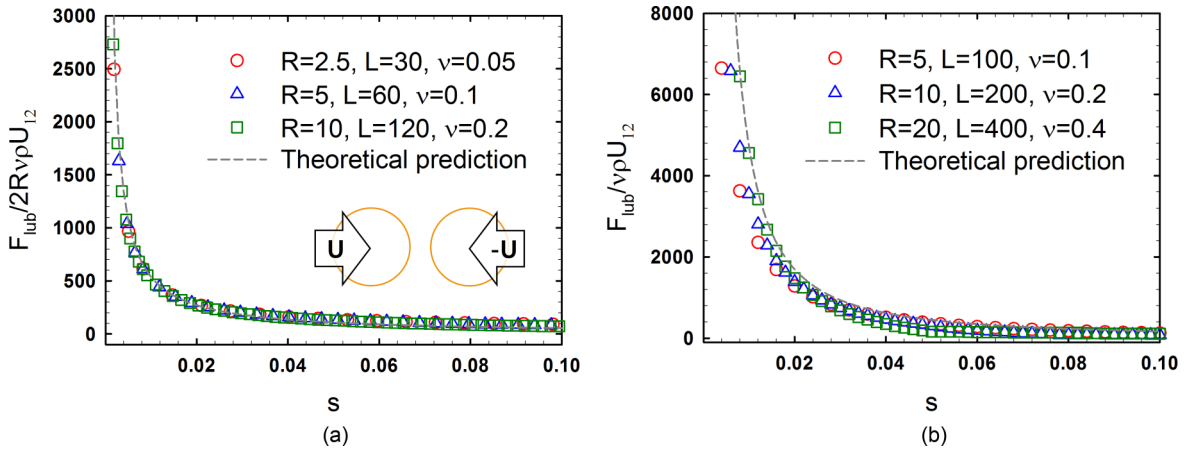

FIG. 3. (Color online) (a) Lubrication force between two identical spheres (3D) for different particle radius, R. The dashed line was obtained from the lubrication theory, Eq. (27). (b) Lubrication force between two identical cylinders (2D) for different particle radius, R.

angular velocity converges to 0.5. This result coincides well with Taylor's analytical solution [36] and that of Kromkamp *et al.* [16] by LBM. From this result, we could confirm that the wall height $H = 400$ in Sec. III A is appropriate to minimize the wall effect in our system. In concentrated particle suspensions, the role of short range hydrodynamic interaction (HI), or the lubrication force among the particles becomes imporatant [7–10]. To confirm the reproducibility of the lubrication force in the present LBM coupled with SPM, the lubrication force between two spheres (3D case) and two cylinders (2D case) moving toward each other at a constant speed was computed in a rectangular channel. The density of the solvent and particle was $\rho = 1$ and $\rho_p = 1$, respectively. Verification was performed at fixed particle Reynolds number, $\mathrm{Re} = U_{12}(2R)/\nu = 0.2$ with a constant relative velocity for two approaching particles, $U_{12} = (U_1 - U_2) = 0.001$. The size of the simulation domain was set to $4R \times 2R \times 2R$ ($R = 2.5-10$ in 3D case) and $4R \times 2R$ ($R = 5-20$ in 2D case), respectively. A periodic boundary condition was imposed on all boundaries, and the tests were peformed with varing particle radii, R, to confirm the dependency of the lattice resolution in our algorithm. In the 3D system, the lubrication force F_{lub} for the two approaching particles was calulated by simulation, and it was comapared with the analytical solution from Eq. (28) [37–39].

$$\frac{F_{\mathrm{lub}}}{2\rho\nu U_{12}/\lambda} = \frac{3\pi}{4s} + C_w. \tag{28}$$

For two spherical particles with the same radius, λ was defined as $1/R$, and s was $d/R - 2$, where d means the center to center distance between the particles. C_w is a constant which depends on the wall, and $C_w = 0$ was used under the assumption of an infinite channel height. As shown in Fig. 3(a), the result coincides well with the theoretical prediction in the 3D system. A 2D simulation was also performed. The F_{lub} values obtained by the simulation are plotted with the analytical solution of Dodd *et al.* [40] in Fig. 3(b). The simulation results matched well with the analytical solution. These results confirm that the lubrication force between two particles (or cylinders) is well represented in SPM-LBM.

C. Relative shear viscosity at low particle Reynolds number

We investigated the viscosity at a particle Reynolds number of $\mathrm{Re_p} = 0.01$, for which the inertia can be neglected. $\mathrm{Re_p}$ means the ratio of the inertia force to the viscous force on a solid particle, and it is defined by Eq. (29).

$$\mathrm{Re_p} = \frac{\dot{\gamma} D^2}{\nu}. \tag{29}$$

The Mach number Ma was kept below 0.1 for a stable calculation under an incompressible fluid assumption [41]. It was defined by Eq. (30), where H denotes the channel height.

$$\mathrm{Ma} = \frac{\dot{\gamma} H}{2c_s}. \tag{30}$$

The initial velocity was set to zero, and the shearing wall boundary condition was adopted. As shown in Fig. 4, the shear flow was imposed in the simulation domain, and the shear stress induced by the interaction between the solid particles and solvent was monitored. The enhanced shear stress was captured for the higher particle volume fraction shown in Figs. 4(d)–4(f).

Next, the shear viscosity of the suspension was quantitatively analyzed for varying particle volume fractions. To measure the shear stress, both wall shear stress (WSS) and the method of planes (MOP) were used. Calculations were performed for 300 000 time steps in each case, and the shear stress was obtained by averaging over 200 000 of the final time steps, where the stress reached a steady state with some fluctuations. We also performed simulations for 4 000 000 time steps, and found that the results (shear stress, viscosity, and local density distribution) are basically the same. Thus we will provide the results only for 300 000 time steps. The shear stress was measured only at the wall in the WSS case; however, it was obtained by averaging the local shear stress in Eq. (27) over all the planes along the gradient direction in MOP. The shear viscosity of the suspension was determined by the shear stress divided by the applied shear rate on the system, and the relative shear viscosity was defined as a ratio of the suspension viscosity and solvent viscosity shown in Eq. (31).

$$\eta_r = \frac{\eta_{\mathrm{suspension}}}{\eta_{\mathrm{solvent}}}. \tag{31}$$

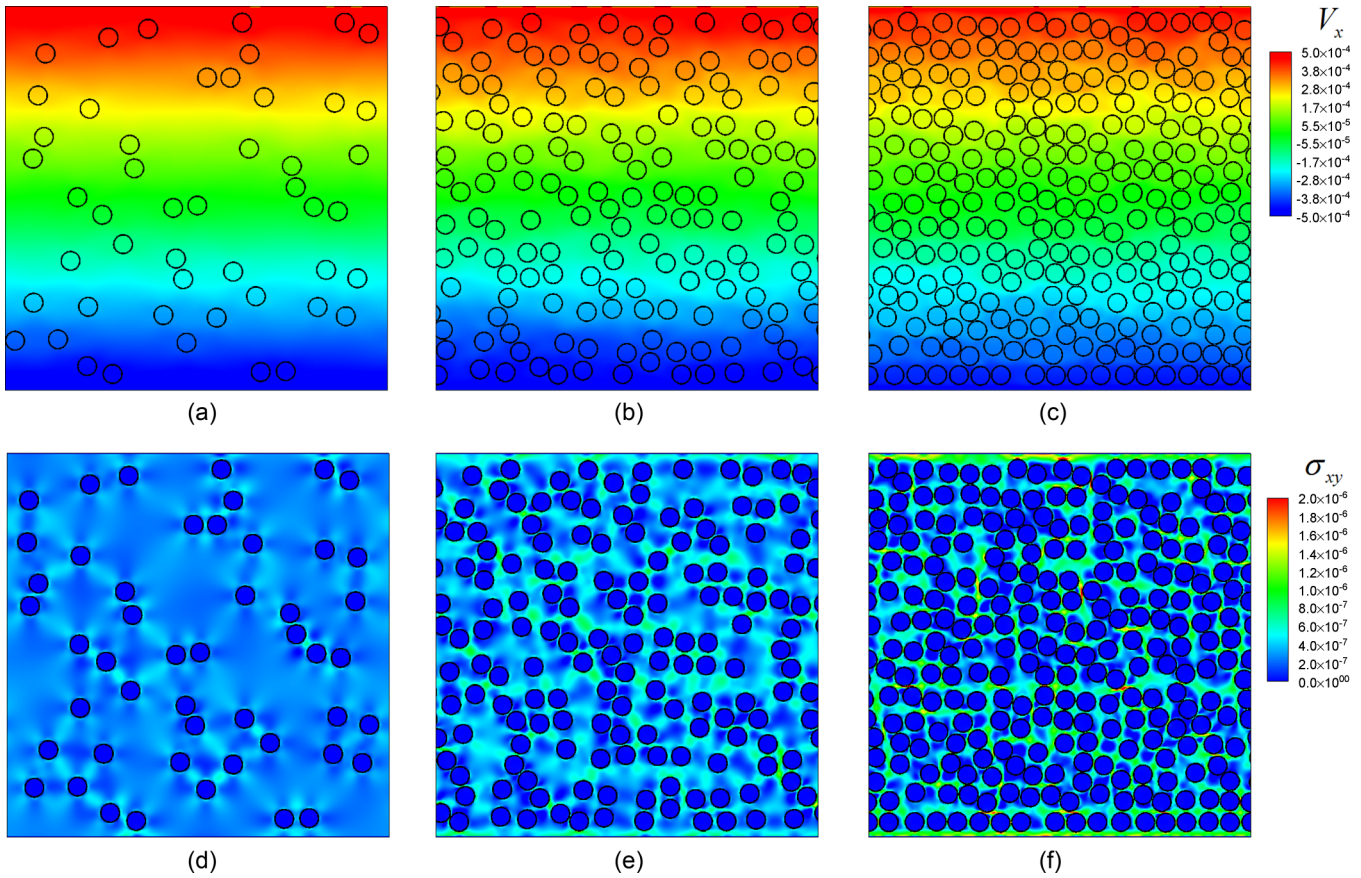

FIG. 4. (Color online) x component of velocity and shear stress (of the solvent) at time step 300 000 ($\mathrm{Re_p} = 0.01$). (a)–(c) denote particle configurations with x component of velocity in color for $\phi = 0.1$, $\phi = 0.3$, and $\phi = 0.5$. (d)–(f) show the distribution of shear stress (of the solvent) for $\phi = 0.1$, $\phi = 0.3$, and $\phi = 0.5$.

Because the shear viscosity was determined in terms of the wall shear rate, it could well be regarded as an apparent shear viscosity.

Nonhomogeneous shear rate is known to develop in the concentrated suspension in the confined system due to the absence of particles near the wall region [16,17]. The shear viscosity which is defined according to the bulk shear rate can be different from the apparent shear viscosity (∼1% for $\mathrm{Re_p} = 0.01$, ∼20% for $\mathrm{Re_p} = 1.0$). The two results may be different to some degree, but the trend itself does not change at all. Therefore, we will use wall shear rate to define the shear viscosity in this study.

The relative shear viscosity is plotted in Fig. 5. For both WSS and MOP, the relative viscosity showed an overshoot followed by a decrease and finally reached a steady state. The results are the same at long times for both cases. The relative shear viscosity can often be predicted by the Krieger-Dougherty equation, Eq. (32), which is a well-known

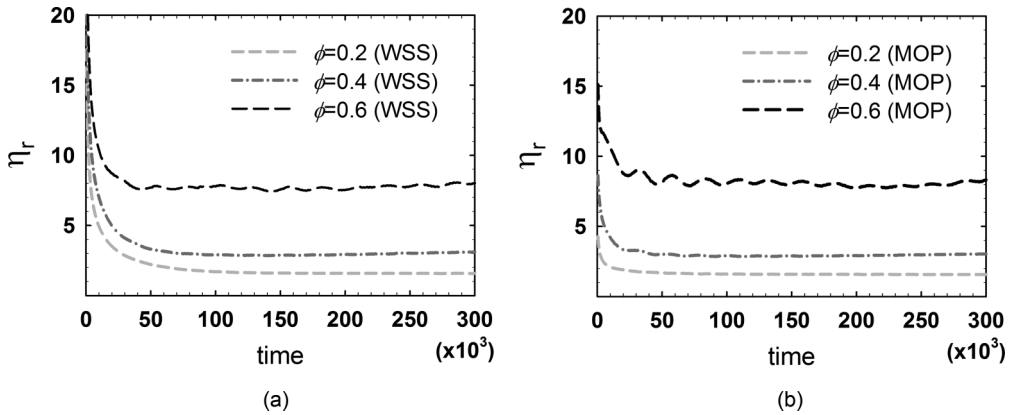

FIG. 5. Relative shear viscosity at different volume fraction of solid particles ($\mathrm{Re_p} = 0.01$). (a) WSS and (b) MOP.

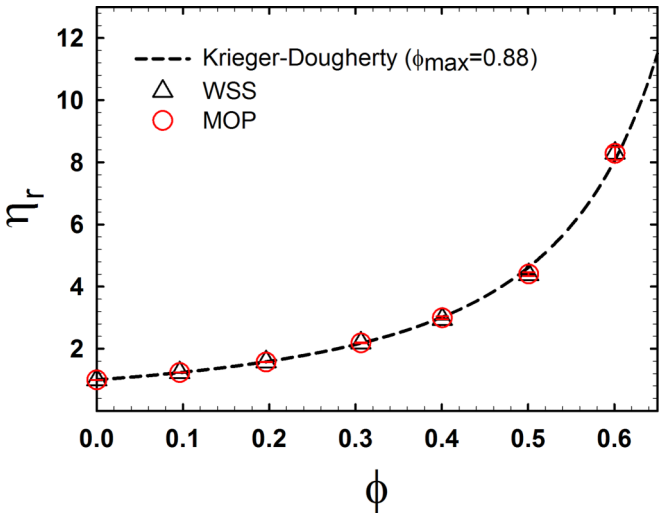

FIG. 6. (Color online) Relative shear viscosity in terms of volume fraction of solid particles ($Re_p = 0.01$). Error bar was obtained by averaging the data from 200 000 to 300 000 time steps (for five simulation sets). Both algorithms (WSS and MOP) predict the Krieger-Dougherty equation very well.

semiempirical model for a particle suspension [42].

$$\eta_r^{\mathrm{KD}} = \left(1 - \frac{\phi}{\phi_{\max}}\right)^{-[\eta]\phi_{\max}}. \tag{32}$$

In Eq. (32), ϕ is the overall particle volume fraction; $\phi_{\max}$ is the maximum packing fraction, and the dimensionless factor $[\eta]$ denotes the intrinsic viscosity of the suspension. In this study, $\phi_{\max} = 0.88$ and $\phi_{\max}[\eta] = 1.82$ were used as in previous experimental and simulation reports [16,43]. Even though the experiment was carried out with 3D particles, it was applicable to both the 2D and 3D suspensions at low Reynolds number as shown in Kromkamp *et al.* [16].

The relative shear viscosity as a function of the particle volume fraction is plotted in Fig. 6. It was evaluated by both WSS and MOP, and the result was obtained by averaging five simulation sets with different initial configurations of solid particles. An increase in the relative shear viscosity was observed with an increase in the particle volume fraction, and the results corresponded well with the Krieger-Dougherty equation for both WSS and MOP. It means that LBM coupled with SPM can be applied to investigate the rheology of particle systems from dilute to concentrated suspensions. Furthermore, it also proves that MOP can be used as an alternative approach to measure the rheological properties in LBM coupled with SPM.

D. Shear thickening at high particle Reynolds number

The rheology of concentrated particle suspensions ($\phi = 0.3-0.6$) was investigated at high particle Reynolds number. Re_p was only controlled by the shear rate, and the other simulation parameters were the same as in Sec. III A. The relative shear viscosity was obtained through the same process as in the previous section, and is plotted in Fig. 7. For all the cases, a strong overshoot was observed at first, and it decreased to equilibrium at around 100 000 time steps. Even though there exists a discrepancy at the initial stage, the predictions by MOP and WSS coincided well for a large strain. In WSS, the shear stress is measured only at the wall boundary, while the shear stress is averaged from the local shear stress obtained at each plane in MOP. This difference may lead to a slightly different stress, especially at the initial stage when the momentum is not fully transferred to the domain.

The increase in the relative shear viscosity at a high shear rate, the so-called shear thickening, was captured with an increase in Re_p; however, the growth rate was different for different volume fractions. For $\phi = 0.4$ shown in Figs. 7(a) and 7(b), a small difference was observed for $Re_p = 0.01$ and $Re_p = 1.0$, but for more concentrated suspensions of $\phi = 0.5$ and 0.6, a highly enhanced relative shear viscosity was observed at high Re_p seen in Figs. 7(c)–7(f).

The total relative shear viscosity showed a strong fluctuation with time, especially in the shear thickening region for both WSS and MOP. When we separated the contribution of each phase, only the particle contribution showed a strong fluctuation in the shear thickening region, in which the solvent contribution was constant at 1.0 shown in Figs. 7(b), 7(d), and 7(f). These results prove that the fluctuation in the total relative shear viscosity originates from the particle contribution. It could be that shear thickening is strongly correlated with the microstructural evolution of the suspension under large deformation as in previous reports [9,10] which will be discussed in the next section.

In Fig. 8, the relative shear viscosity is plotted in terms of Re_p. The increase in shear viscosity and shear thickening was clearly captured, and the results by both WSS and MOP coincided well with each other. In Table II, the values for the relative shear viscosity are compared. At $\phi = 0.3$, the difference in the relative shear viscosity at $Re_p = 0.005$ and $Re_p = 2.0$ was 0.3059 (WSS) and 0.2958 (MOP). In this case, both results from WSS and MOP were well matched, but shear thickening was not strong. However, for higher particle volume fractions of $\phi = 0.4-0.6$, shear thickening was more pronounced. Differences in the shear viscosity between $Re_p = 0.005$ and $Re_p = 2.0$ was as follows: for $\phi = 0.4$, 0.8387 (WSS) and 0.8146 (MOP); for $\phi = 0.5$, 1.9798 (WSS) and 1.9985 (MOP), and for $\phi = 0.6$, 4.4340 (WSS) and 4.5485 (MOP). It is well known that shear thickening is more pronounced for more concentrated and higher shear rate systems [6,9,14], and our simulation corresponds well with previous experimental and numerical studies. Furthermore, the results obtained by both WSS and MOP match well with each other, which also means that we can use MOP as an alternative method to measure the shear stress (or shear viscosity) in LBM coupled with SPM.

E. Microstructure

In the previous section, the shear viscosity was evaluated by both the WSS and MOP. Shear thickening was successfully captured, but the origin of the shear thickening is still less clear. Therefore, we tried to explain shear thickening from a microstructural change in the suspensions. First, the pair-distribution function for the particle configuration was investigated in the shear-gradient ($x - y$) plane because the non-Newtonian behavior of the particle system is closely related with the anisotropy in the pair-distribution function

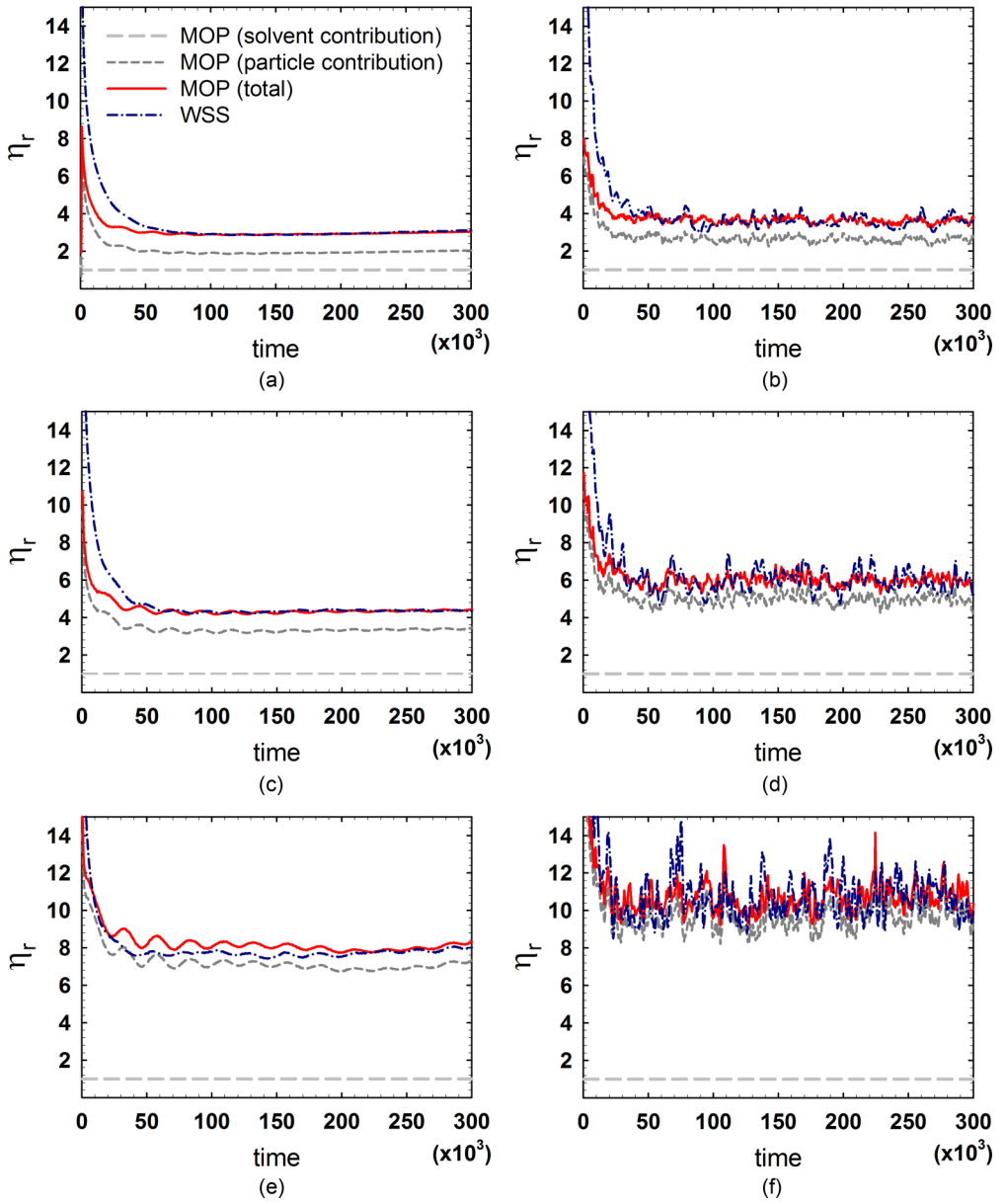

FIG. 7. (Color online) Relative viscosity measured by wall shear stress (WSS) and by the method of planes (MOP): (a) $\phi = 0.4$, $\mathrm{Re_p} = 0.01$; (b) $\phi = 0.4$, $\mathrm{Re_p} = 1.0$; (c) $\phi = 0.5$, $\mathrm{Re_p} = 0.01$; (d) $\phi = 0.5$, $\mathrm{Re_p} = 1.0$; (e) $\phi = 0.6$, $\mathrm{Re_p} = 0.01$; and (f) $\phi = 0.6$, $\mathrm{Re_p} = 1.0$.

[10]. The pair-distribution function for $\phi = 0.6$ at various particle Reynolds numbers is plotted in Fig. 9. In Fig. 9(a), the pair-distribution function at low $\mathrm{Re_p}$ ($\mathrm{Re_p} = 0.01$) is plotted. In this case, a strong intensity to the flow direction is clearly observed, which means that most particles are aligned to the flow direction under the shear flow. If the system is dominated

TABLE II. Relative shear viscosity which was measured by wall shear stress (WSS) and the method of planes (MOP).

	$\mathrm{Re_p} = 0.005$	$\mathrm{Re_p} = 0.01$	$\mathrm{Re_p} = 0.1$	$\mathrm{Re_p} = 1.0$	$\mathrm{Re_p} = 2.0$
$\phi = 0.3$ (WSS)	2.1762	2.1897	2.4356	2.3819	2.4821
$\phi = 0.4$ (WSS)	2.8945	3.0826	3.4766	3.6098	3.7332
$\phi = 0.5$ (WSS)	4.3476	4.3854	5.3655	6.0123	6.3274
$\phi = 0.6$ (WSS)	7.7917	7.8427	9.4512	10.8428	12.2257
$\phi = 0.3$ (MOP)	2.1747	2.1905	2.4452	2.4130	2.4705
$\phi = 0.4$ (MOP)	2.9120	3.0404	3.3956	3.6146	3.7266
$\phi = 0.5$ (MOP)	4.3043	4.4066	5.5489	5.9823	6.3028
$\phi = 0.6$ (MOP)	7.6391	7.9973	9.4619	10.7896	12.1876

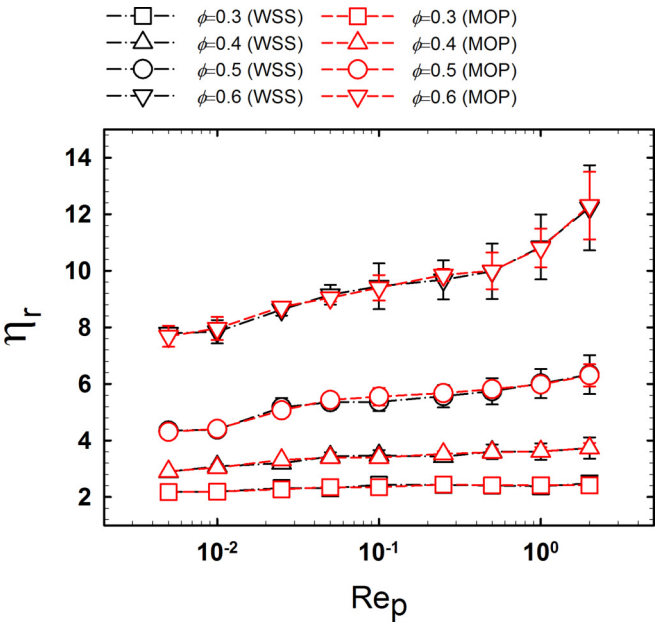

FIG. 8. (Color online) Shear viscosity as a function of particle Reynolds number. Increase of relative shear viscosity was observed at high particle Reynolds number $\mathrm{Re_p}$. The results from WSS and MOP are matched well with each other (error bar was obtained by time average from 200 000 to 300 000 time steps for five simulation sets which have different initial particle configurations).

by the Brownian motion, the particle alignment is suppressed by self-diffusion, and the isotopic pair-distribution function is obtained [9]. However, an anisotropic particle distribution was observed even at low $\mathrm{Re_p}$ as small as 0.01 because our system corresponds to the hydrodynamics dominant region where the Brownian motion is negligible. As shown in Figs. 9(b) and 9(c), a more orientated structure to the compressive axis was observed at high $\mathrm{Re_p}$. In other words, more particles were aligned to the compressive axis at a higher shear rate. It is well known that the structural change of the particles is related with non-Newtonian behavior such as shear thinning and shear thickening [9,10]. In particular, the particle alignment in the compressive axis was strongly correlated with shear thickening in hard-sphere suspensions, which was well explained by the simulation studies with Stokesian dynamics (SD). In this regard, our simulation confirms the results of previous reports.

The increase in particle distribution in the compressive axis means that the particles come closer in that direction, which facilitates the formation of clusters [7]. The relationship between shear thickening and particle clusters has been widely reported in both experiments [4–6] and numerical studies [7,8,15]. D'Haene *et al.* observed particle clustering in the shear thickening region by rheo-optical studies [4]. Cheng *et al.* reported a particle structure in both shear thinning and shear thickening regimes [6]. They directly observed cluster formation along the compressive axis in a shear thickening regime by fast confocal microscopy, and they confirmed that shear thickening is related with the size of the clusters at a high Péclet number. Brady and Bossis [7] related shear thickening of Brownian hard-sphere suspensions with particle clustering, which are the so-called hydroclusters in a suspension. They argued that more clusters can be formed by a strong lubrication force among the particles at a high Péclet number, which leads to shear thickening. Raiskinmäki *et al.* [15] investigated shear thickening of non-Brownian suspensions by LBM, and reported a relationship between the probability of the clustering of particles and the shear thickening intensity. They confirmed that the number of clusters as well as their size increases with $\mathrm{Re_p}$ in the shear thickening region. Even though previous studies dealt with systems with minor differences between each other, they all concluded that the formation of clusters can trigger shear thickening in suspensions.

We also carried out an analysis to confirm the relationship between shear thickening and cluster formation. In our analysis, a cluster was defined as a group which has more than one bond among the particles. The bond was counted when the surface to surface distance of the particles was lower than 4% of the particle diameter, which was determined from the first peak in the pair distribution of the particles. The particle configuration at time step 300 000 is plotted in Fig. 10. The particles included in the same cluster were marked with the same color. Here, the particles with a white color denote the ones belonging to the largest cluster, while the particles with a black color are the individual particles which are not included in the cluster. As seen in Fig. 10, a small amount of clusters was formed at $\mathrm{Re_p} = 0.01$ even at a high particle volume fraction, but more clusters were observed at higher $\mathrm{Re_p}$. In particular, in the case of $\phi = 0.6$ in Figs. 10(c) and 10(f), the formation of a larger cluster is clearly observed with the increase in $\mathrm{Re_p}$. At the same time, most clusters aligned in the compressive axis, which explains qualitatively

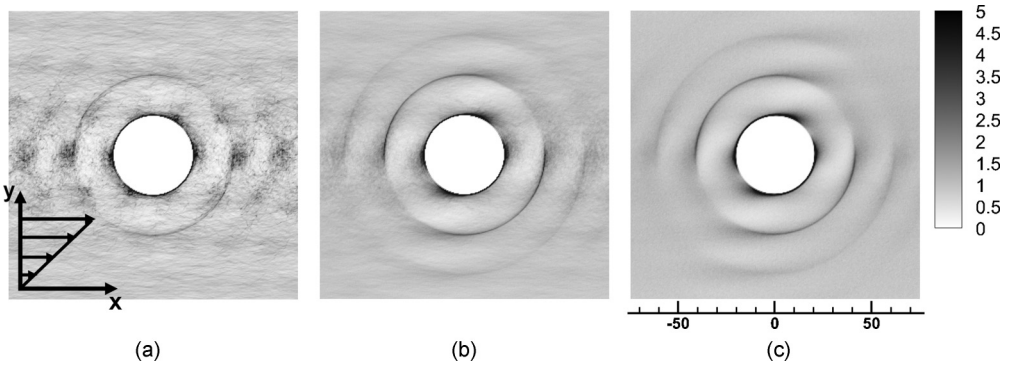

FIG. 9. Time averaged pair-distribution function for $\phi = 0.6$. (a) $\mathrm{Re_p} = 0.01$, (b) $\mathrm{Re_p} = 0.01$, and (c) $\mathrm{Re_p} = 1.0$. Abscissa denotes flow direction and ordinate denotes gradient direction. Darker region represents higher probability to find particles.

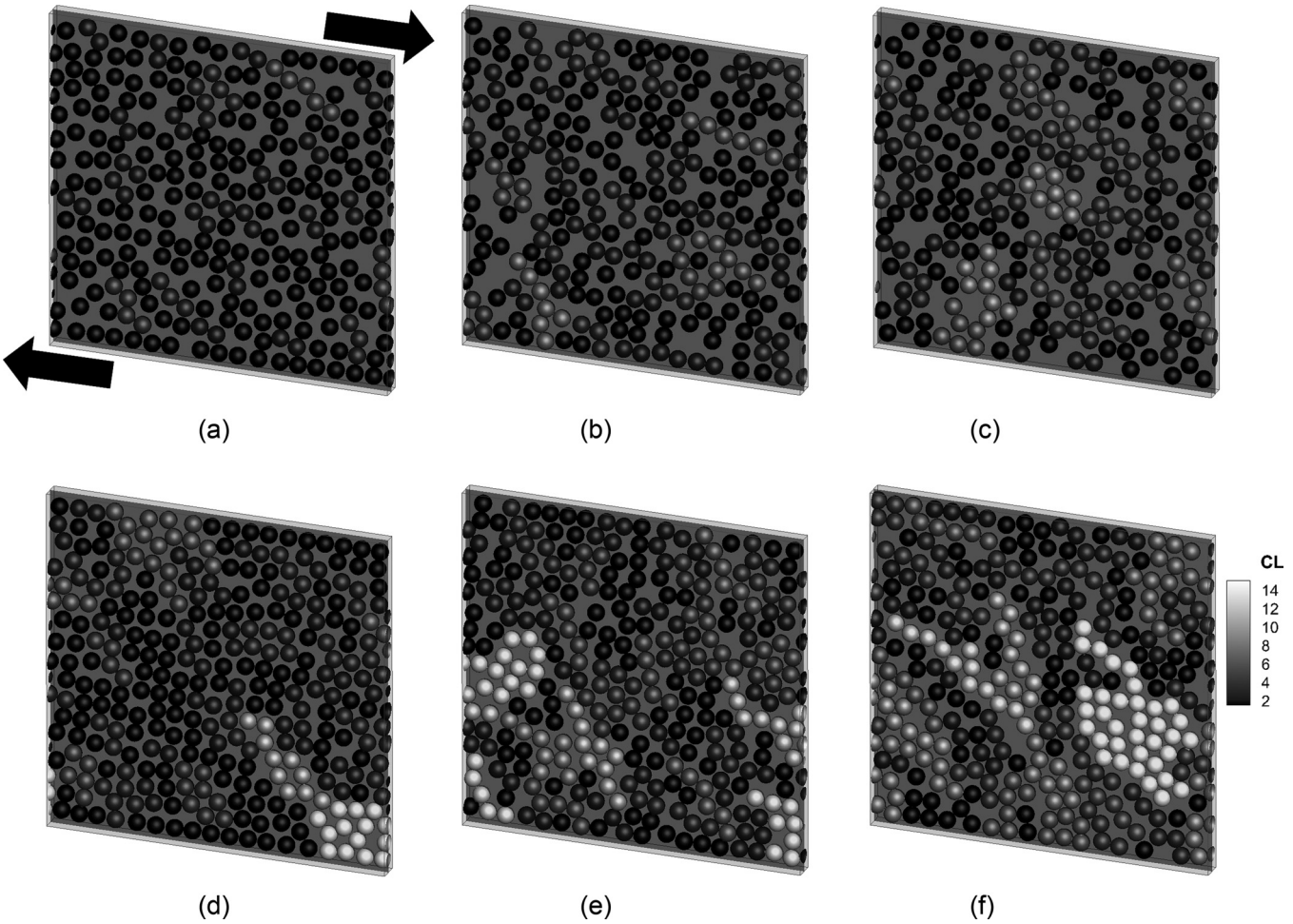

FIG. 10. Particle configuration at time step 300 000. (a) $\phi = 0.5$, $\mathrm{Re_p} = 0.01$; (b) $\phi = 0.5$, $\mathrm{Re_p} = 0.1$; (c) $\phi = 0.5$, $\mathrm{Re_p} = 1.0$; (d) $\phi = 0.6$, $\mathrm{Re_p} = 0.01$; (e) $\phi = 0.6$, $\mathrm{Re_p} = 0.1$; and (f) $\phi = 0.6$, $\mathrm{Re_p} = 1.0$. The particles in the same cluster have the same color. Nonclustering particles are black, and the particles in the larger cluster are close to white.

well the anisotropy in the pair-distribution function shown in Fig. 9.

The size distribution of the clusters was quantitatively analyzed too. Here, the number of particles N and the probability P_N were calculated to find clusters that consist of N particles. The results were obtained by averaging the values from the simulation time 200 000 to 300 000 for five simulation sets with different initial configurations. Graphs in terms of P_N and N are shown in Fig. 11. In Fig. 11(a) where $\phi = 0.4$, only a small amount of clusters was formed even at high $\mathrm{Re_p}$, but more clusters were observed at a higher volume fraction. This was more pronounced at higher $\mathrm{Re_p}$ shown in Fig. 11(b). The increase in cluster size at high $\mathrm{Re_p}$ was in accordance with the shear thickening behavior in Fig. 8, which coincides well with

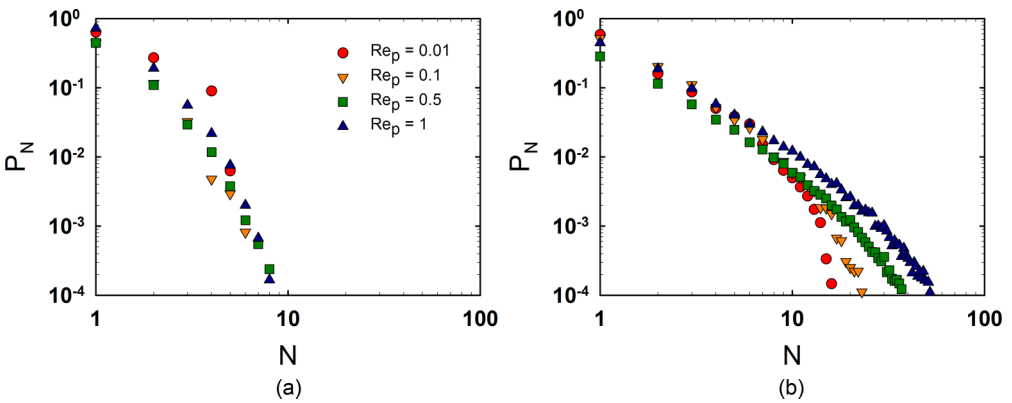

FIG. 11. (Color online) Time averaged probability of the number of solid particles in clusters. (a) $\phi = 0.4$ and (b) $\phi = 0.6$. Larger clusters were formed with an increase in particle Reynolds number at higher volume fraction.

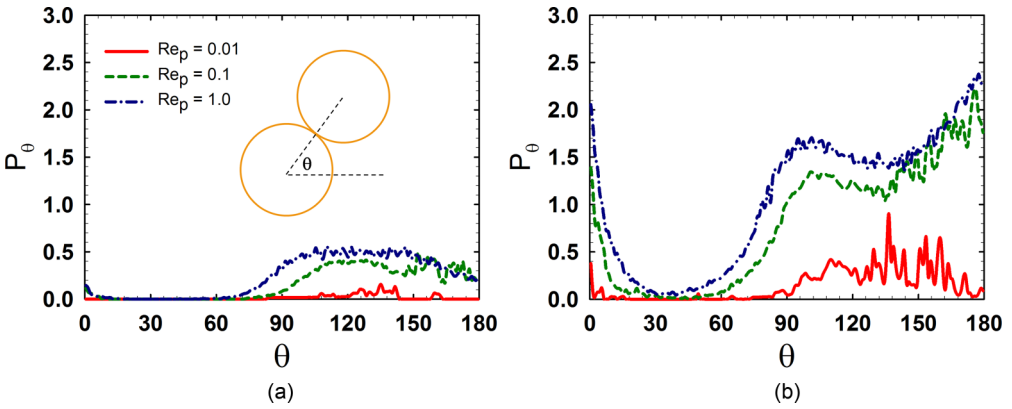

FIG. 12. (Color online) Time averaged angular distribution of clusters. (a) $\phi = 0.4$ and (b) $\phi = 0.6$. Higher angular distribution was observed over 90°, which means that the clusters are aligned to the compressive axis.

previous reports from both experiments [4–6] and simulation studies [7,8,15]. Especially, the increase in cluster distribution is qualitatively similar to the results of Cheng *et al.* [6]. Even though they studied Brownian suspensions, both results show a resemblance in terms of the formation of clusters in the hydrodynamic force dominant region.

The orientation of clusters was also checked in terms of the angular distribution of the particles which are included in the clusters. The angle between two particles in cluster θ was calculated by Eq. (33) in terms of the center to center distance r_{ij} and the y component of the vector $X_{i,y} - X_{j,y}$ for the i and j particles.

$$\theta = \tan^{-1}\left(\frac{X_{i,y} - X_{j,y}}{r_{ij}}\right). \tag{33}$$

Time averaged probability is plotted in Fig. 12. Here, P_θ denotes the angular distribution of the particles within a cluster. A $\theta < 90^\circ$ describes a region of extension, and a $\theta > 90^\circ$ means a region of compression in the flow direction. For $\phi = 0.4$, the distribution was lower than that of $\phi = 0.6$ shown in Fig. 11, and the angular distribution increased at higher $\mathrm{Re_p}$ for all the cases. For a more concentrated system such as $\phi = 0.6$,

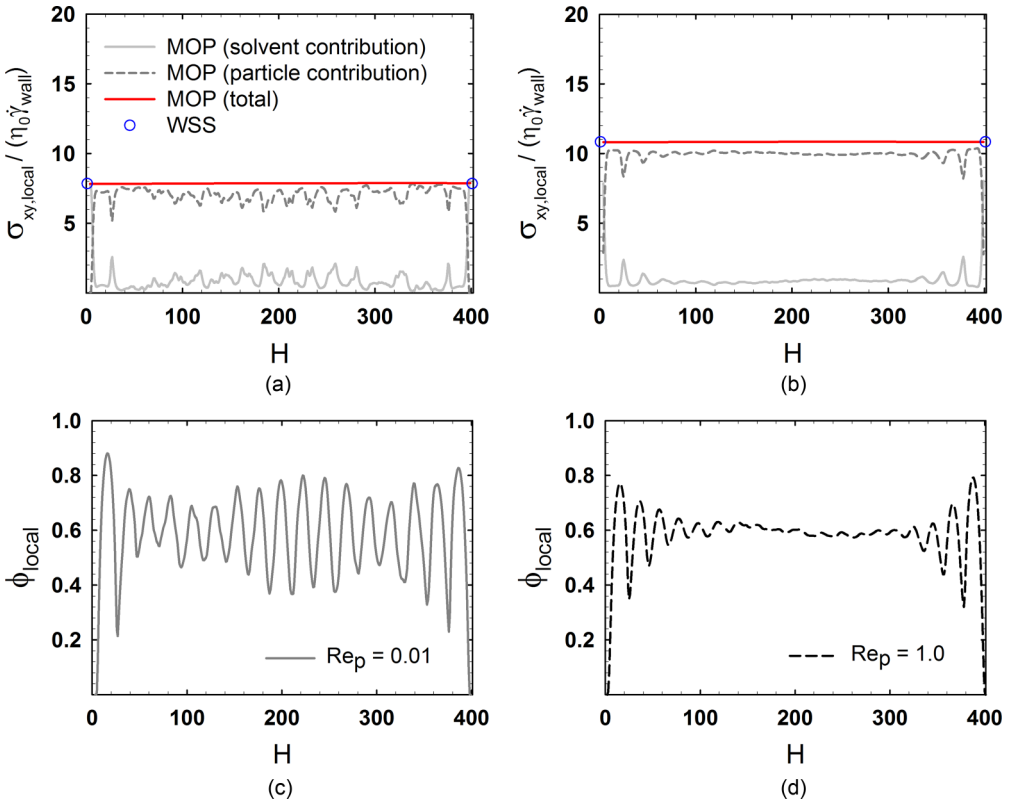

FIG. 13. (Color online) Time averaged (from 200 000 to 300 000) local shear stress measured by the method of planes (MOP) to the gradient direction for $\phi = 0.6$: (a) $\mathrm{Re_p} = 0.01$ and (b) $\mathrm{Re_p} = 1.0$. Time averaged particle volume (area) fraction: (c) $\mathrm{Re_p} = 0.01$ and (d) $\mathrm{Re_p} = 1.0$.

an increase in the distribution was clearly observed, which means that more particles were aligned in the compressive axis with clustering. This can be related to the particle alignment which was described in Figs. 9 and 10, and it also coincides with previous reports in both experiments [6] and numerical studies [7–9,17].

F. Correlation between local shear stress and local particle volume fraction

As already mentioned, shear thickening is closely related to the increase in clusters at high particle Reynolds number $\mathrm{Re_p}$. The bulk rheology is strongly affected by the structural change of the suspension, especially by the formation of clusters. However, it is still unclear how the local structure of the material affects the local rheology, and changes the bulk rheology. There exist few reports on the correlation between local rheology and local structure of a suspension because it is hard to directly measure the local rheology of a material either by experiments or by simulation due to many technical limitations. We adopted the method of planes (MOP) [20] which was recently introduced to access the local dynamics of a suspension. In our system, the shear stress in each plane along the gradient direction was defined as the local shear stress [35], and it was obtained by the summation of the shear stress of solvent and that of the particles which was locally measured by Eqs. (23)–(27).

First, the time averaged solvent and particle contributions to the total shear stress were locally calculated along the channel height, and the results are compared with WSS in Figs. 13(a) and 13(b). Here, we described the local shear stress as normalized by the shear rate at the moving wall $\dot{\gamma}_{\mathrm{wall}}$ multiplied by the solvent viscosity η_0. Under the assumption that the local shear rate is the same with the shear rate near the wall, the normalized shear stress can be explained as the relative shear rate. The time averaged local shear stress by MOP coincided well with that measured by WSS, and shear thickening at high $\mathrm{Re_p}$ was also captured. In the particle

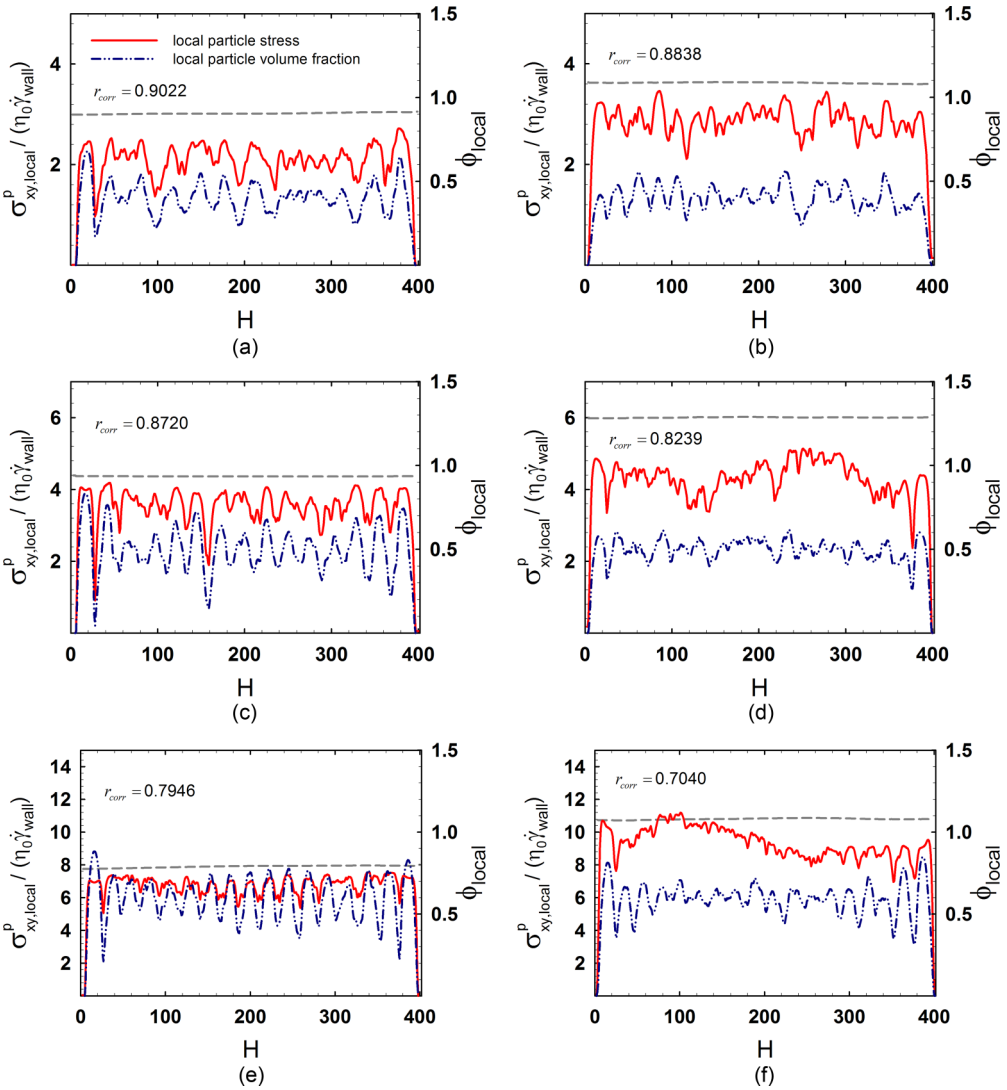

FIG. 14. (Color online) Local particle stress and local particle volume fractions at $t = 300{,}000$. (a) $\phi = 0.4$, $\mathrm{Re_p} = 0.01$; (b) $\phi = 0.4$, $\mathrm{Re_p} = 1.0$; (c) $\phi = 0.5$, $\mathrm{Re_p} = 0.01$; (d) $\phi = 0.5$, $\mathrm{Re_p} = 1.0$; (e) $\phi = 0.6$, $\mathrm{Re_p} = 0.01$; and (f) $\phi = 0.6$, $\mathrm{Re_p} = 1.0$. Dashed line (medium dash, light gray) above the local stress line denotes time averaged local stress (total) which was normalized by the shear viscosity of pure solvent multiplied by wall shear rate.

contribution measured by MOP, a fluctuation exists near the wall, which might be correlated with the density distribution of the particles near the wall. To confirm this, the particle volume fraction was locally measured. The local particle volume (area in 2D) fraction was calculated by the smoothed profile function in Eq. (5). After summing the smoothed profile functions at the LBM nodes in each plane, it was divided by the surface area (length in 2D) of each plane. Then, the local particle volume (area) fraction in each plane could be obtained.

The time averaged local particle volume (surface area in 2D system) fraction is plotted in Figs. 13(c) and 13(d) in terms of the channel height H. For all the cases, a strong concentration fluctuation was observed near the wall, and it looks qualitatively similar to the results in previous experimental [6] and simulation studies [14,16,17]. The fluctuation of the local particle volume fraction in Figs. 13(c) and 13(d) was well reflected in the particle contribution to the local shear stress shown in Figs. 13(a) and 13(b), and these results show how MOP captures the local shear stress upon microstructural changes. We now focus on the local shear stress at specific times because the local rheology could be constantly changing due to the structural evolution of the suspension during the flow. The data at simulation time step 300 000 were chosen as representative for which the cluster formation was clearly captured with shear thickening shown in Fig. 10. The normalized local particle stress (the particle contribution in local shear stress) and local particle volume fraction at time step 300 000 are plotted in Fig. 14. At high $\mathrm{Re_p}$, an increase in the local shear stress was observed, and this was enhanced for a more concentrated system and for higher $\mathrm{Re_p}$ shown in Fig. 8. Of note is the correlation between the local shear stress and local particle volume fraction. At low $\mathrm{Re_p}$ where shear thickening did not occur, the fluctuation for both the local shear stress and local particle volume fraction looks similar as shown in Figs. 14(a), 14(c), and 14(e). However, as seen in Figs. 14(b), 14(d), and 14(f), the correlation between the local shear stress and local volume fraction decreased at high $\mathrm{Re_p}$ ($\mathrm{Re_p} = 1.0$), which is more clearly observed at a higher particle volume fraction.

Correlations between the local shear stress and the local particle volume fraction can be quantitatively analyzed by Pearson's correlation coefficient [44]. It is denoted as r_{corr} and is defined by Eq. (34). Here, $\phi_{i,\mathrm{local}}$ and $\sigma^{p}_{xy,i,\mathrm{local}}$ mean the local particle volume fraction and the local particle stress in plane i, and $\bar{\phi}_{\mathrm{local}}$ and $\bar{\sigma}^{p}_{xy,i,\mathrm{local}}$ are the averaged values over all the planes.

$$r_{\mathrm{corr}} = \frac{\sum(\phi_{i,\mathrm{local}} - \bar{\phi}_{\mathrm{local}})(\sigma^{p}_{xy,i,\mathrm{local}} - \bar{\sigma}^{p}_{xy,i,\mathrm{local}})}{\left[\sum\left(\phi_{i,\mathrm{local}} - \bar{\phi}_{\mathrm{local}}\right)^2 \sum\left(\sigma^{p}_{xy,i,\mathrm{local}} - \bar{\sigma}^{p}_{xy,i,\mathrm{local}}\right)^2\right]^{0.5}}. \tag{34}$$

When the linear correlation is strong, r_{corr} is close to 1, and it reduces to 0 when there is no correlation. The Pearson's correlation coefficient r_{corr} between the local particle stress and the local volume fraction is plotted in Fig. 15. For $\phi = 0.4$, r_{corr} was 0.9022 at $\mathrm{Re_p} = 0.01$ and 0.8838 at $\mathrm{Re_p} = 1.0$. There exists a strong linear correlation, even though it slightly decreases at high $\mathrm{Re_p}$. For more concentrated suspensions, a reduction of r_{corr} was observed. In the case of $\phi = 0.5$,

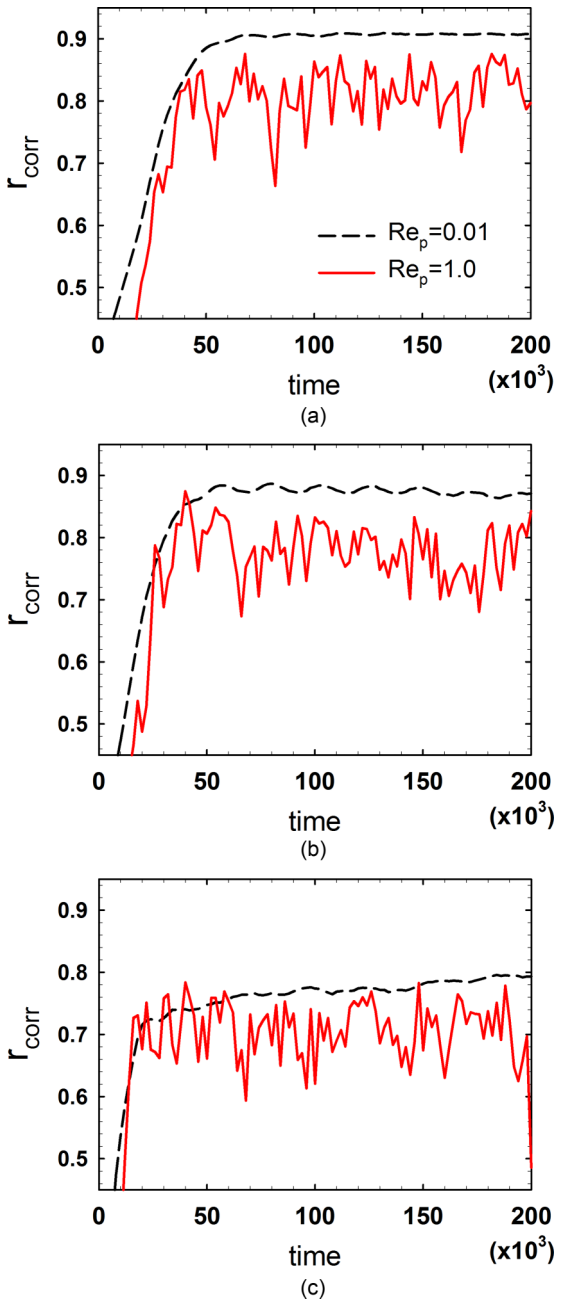

FIG. 15. (Color online) Pearson's correlation coefficient between local particle stress and local particle volume fractions as a function of time. (a) $\phi = 0.4$, (b) $\phi = 0.5$ and (c) $\phi = 0.6$.

r_{corr} was 0.8720 at $\mathrm{Re_p} = 0.01$ and 0.8239 at $\mathrm{Re_p} = 1.0$. In the case of $\phi = 0.6$, r_{corr} was 0.7946 at $\mathrm{Re_p} = 0.01$ and 0.7040 at $\mathrm{Re_p} = 1.0$. It clearly shows that a linear correlation between the local particle stress and the local particle volume fraction decreases for more concentrated suspensions at a high shear rate. For every 2000 time steps, the correlation between the local particle stress and the local particle volume fraction was calculated by Eq. (34), and r_{corr} is plotted as a function of time in Fig. 15. At the initial stage, a low r_{corr} was observed for all the cases; however, it gradually increased after some time. A low r_{corr} at the initial stage can be understood as the progress of the shear stress (or shear viscosity) growth. As shown in

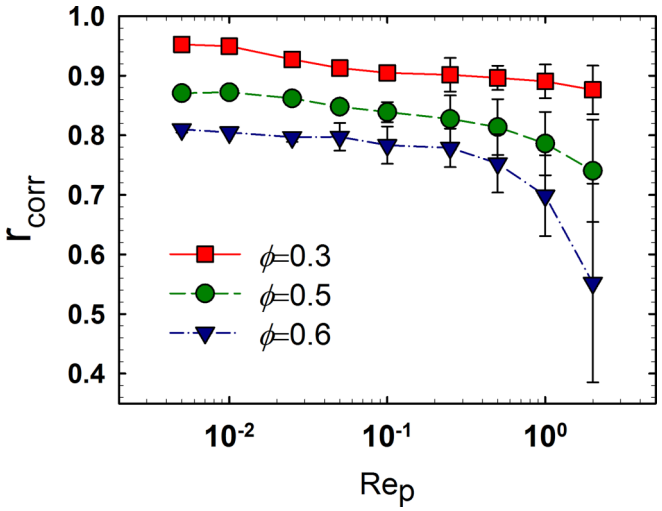

FIG. 16. (Color online) Time averaged Pearson's correlation coefficient between local particle stress and local particle volume fraction. The correlation decreases with the increase in local particle volume fraction and particle Reynolds number, $\mathrm{Re_p}$.

Figs. 5 and 7, viscosity overshoot was predicted at the initial stage, and then, it equilibrated after enough strain. This could be related with the sudden momentum exchange near the wall boundary in LBM, and this is also verified in r_{corr} in Fig. 15. The increase of r_{corr} looks proportional to the particle volume fraction because the probability to form clusters increases due to the reduced distance among the particles. At low $\mathrm{Re_p}$, a relatively high r_{corr} was observed with weak fluctuation, but the decrease of r_{corr} was observed at high $\mathrm{Re_p}$ with a strong fluctuation. The fluctuation in r_{corr} looks similar to that in the relative shear viscosity which was shown in Fig. 7, and it could be related with the microstructural change, especially cluster formation at high $\mathrm{Re_p}$.

To more clearly understand the effect of $\mathrm{Re_p}$ on the linear correlation between the local particle stress and the local particle volume fraction, the time averaged Pearson's correlation coefficient r_{corr} was plotted as a function of the $\mathrm{Re_p}$ in Fig. 16. r_{corr} decreased with an increase in the particle volume fraction, and it also decreased with $\mathrm{Re_p}$. When shear thickening was not strong, a slight decrease in r_{corr} was observed at low $\mathrm{Re_p}$, while it showed a sharp decrease at high $\mathrm{Re_p}$ with shear thickening. It means that, even though the particles occupied the same amount of space, they can show different rheology depending on their microstructure. Local structural change at higher $\mathrm{Re_p}$ could be related with cluster formation shown in Figs. 10 and 11. It is hard to strictly argue that cluster formation during shear thickening is a key factor in reducing the correlation between the local particle stress and the local particle volume fraction yet, but we could confirm that the local rheology of the suspension that originates from the local microstructural change affects the bulk rheology of the suspension.

IV. CONCLUSIONS

The dynamics of a non-Brownian suspension was investigated by the lattice Boltzmann method (LBM) coupled with the smoothed profile method (SPM). The method of planes (MOP) was adopted in SPM to measure the local shear stress, and we confirmed that the results by MOP matched well with those by the wall shear stress (WSS). At low particle Reynolds number, both results followed the Krieger-Dougherty equation, and we confirmed that the present algorithm is promising in studying suspension rheology. At high particle Reynolds number, an increase in the relative shear viscosity, which is the so-called shear thickening, was observed. To correlate the rheology and microstructure of the suspension, we performed various structural analyses. According to the pair-distribution function, more particles were aligned in the compressive axis as the particle Reynolds number increased. By analyzing the cluster size and angular distribution, we observed that larger clusters were formed at high particle Reynolds number, and they were aligned in the compressive axis with shear thickening. The local rheology and local microstructure of the suspension were also investigated by the MOP algorithm. The time averaged local shear stress by MOP coincided well with that measured by WSS, and shear thickening at high $\mathrm{Re_p}$ was also captured. With an increase in the particle Reynolds number, shear thickening was enhanced with more fluctuations in the local shear stress. The local stress fluctuation could be correlated with local microstructural changes of the suspension, and a linear correlation between the local particle stress and the local particle volume fraction was investigated by Pearson's correlation coefficient. When shear thickening was not strong, the Pearson's correlation coefficient maintained a value close to 1, which means that they have a strong linear correlation with each other. On the other hand, a significant decrease in the Pearson's correlation coefficient was observed with shear thickening. This result means that even though the particles occupied the same amount of space, they can show different rheologies depending on their microstructure. It is clear that the local rheology of a suspension, which originates from a local microstructural change, affects the bulk rheology of a suspension. We believe this work provides good inspiration on how to access the local dynamics of suspensions and analyze them.

ACKNOWLEDGMENT

This work was supported by the National Research Foundation of Korea (NRF) Grant No. 2013R1A2A2A07067387, funded by the Korea government (MEST).

[1] R. G. Larson, *The Structure and Rheology of Complex Fluids* (Oxford University Press, New York, 1999).
[2] R. L. Hoffman, J. Rheol. **42**, 111 (1998).
[3] Y. S. Lee and N. J. Wagner, Rheol. Acta **42**, 199 (2003).
[4] P. D'Haene, J. Mewis, and G. G. Fuller, J. Colloid Interface Sci. **156**, 350 (1993).
[5] B. J. Maranzano and N. J. Wagner, J. Chem. Phys. **117**, 10291 (2002).

[6] X. Cheng, J. H. McCoy, J. N. Israelachvili, and I. Cohen, Science **333**, 1276 (2011).
[7] J. F Brady and G. Bossis, J. Fluid Mech. **155**, 105 (1985).
[8] G. Bossis and J. F. Brady, J. Chem. Phys. **91**, 1866 (1989).
[9] D. R. Foss and J. F. Brady, J. Fluid Mech. **407**, 167 (2000).
[10] A. Sierou and J. F. Brady, J. Rheol. **46**, 1031 (2002).
[11] W. R. Hwang, M. A. Hulsen, and H. E. H. Meijer, J. Comput. Phys. **194**, 742 (2004).
[12] S. Succi, *The Lattice-Boltzmann Equation* (Oxford University Press, Oxford, 2001).
[13] C. K. Aidun and J. R. Clausen, Annu. Rev. Fluid Mech. **42**, 439 (2010).
[14] A. Shakib-Manesh, P. Raiskinmäki, A. Koponen, M. Kataja, and J. Timonen, J. Stat. Phys. **107**, 67 (2002).
[15] P. Raiskinmäki, J. A. Åström, M. Kataja, M. Latva-Kokko, A. Koponen, A. Jäsberg, A. Shakib-Manesh, and J. Timonen, Phys. Rev. E **68**, 061403 (2003).
[16] J. Kromkamp, D. van den Ende, D. Kandhai, R. van der Sman, and R. Boom, Chem. Eng. Sci. **61**, 858 (2006).
[17] P. Kulkarni and J. Morris, Phys. Fluids **20**, 040602 (2008).
[18] G. K. Batchelor, J. Fluid Mech. **41**, 545 (1970).
[19] S. Jafari, R. Yamamoto, and M. Rahnama, Phys. Rev. E **83**, 026702 (2011).
[20] T. Krüger, F. Varnik, and D. Raabe, Philos. Trans. R. Soc. A **369**, 2414 (2011).
[21] Y. H. Qian, D. D'Humières and P. Lallemand, Europhys. Lett. **17**, 479 (1992).
[22] A. J. C. Ladd, J. Fluid Mech. **271**, 285 (1994).
[23] N. Q. Nguyen and A. J. C. Ladd, Phys. Rev. E **66**, 046708 (2002).
[24] C. K. Aidun, Y. Lu, and E. J. Ding, J. Fluid Mech. **373**, 287 (1998).
[25] T. Krüger, F. Varnik, and D. Raabe, Comput Math Appl. **61**, 3485 (2011).
[26] Y. Sui, Y. T. Chew, P. Roy, and H. T. Low, J. Comput. Phys. **227**, 6351 (2008).
[27] Y. Nakayama and R. Yamamoto, Phys. Rev. E **71**, 036707 (2005).
[28] K. Kim, Y. Nakayama, and R. Yamamoto, Phys. Rev. Lett. **96**, 208302 (2006).
[29] J. J. Molina, Y. Nakayama, and R. Yamamoto, Soft Matter **9**, 4923 (2013).
[30] S. K. Doddi and P. Bagchi, Int. J. Multiphase Flow. **34**, 966 (2008).
[31] H. C. Andersen, D. Chandler, and J. D. Weeks, Adv. Chem. Phys. **34**, 105 (1976).
[32] B. D. Todd, D. J. Evans, and P. J. Daivis, Phys. Rev. E **52**, 1627 (1995).
[33] F. Varnik, J. Baschnagel, and K. Binder, J. Chem. Phys. **113**, 4444 (2000).
[34] T. Krüger, F. Varnik, and D. Raabe, Phys. Rev. E **79**, 046704 (2009).
[35] T. Krüger, *Computer Simulation Study of Collective Phenomena in Dense Suspensions of Red Blood Cells under Shear* (Springer, Berlin, 2012).
[36] G. I. Taylor, Philos. Trans. R. Soc. A **138**, 41 (1932).
[37] R. G. Cox, Int J. Multiphase Flow **1**, 343 (1974).
[38] I. L. Claeys and J. F. Brady, Physicochem. Hydrodyn. **11**, 261 (1989).
[39] E. J. Ding and C. K. Aidun, J. Stat. Phys. **112**, 685 (2003).
[40] T. L. Dodd, D. A. Hammer, A. S. Sangani, and D. L. Koch, J. Fluid Mech. **293**, 147 (1995).
[41] X. He and L. S. Luo, J. Stat. Phys. **88**, 927 (1997).
[42] I. M. Krieger and T. J. Dougherty, Trans. Soc. Rheol. **3**, 137 (1959).
[43] R. J. Phillips, R. C. Armstrong, R. A. Brown, A. L. Graham, and J. R. Abbott, Phys. Fluids A **4**, 30 (1992).
[44] J. L. Rodgers and W. A. Nicewander, Am. Stat. **42**, 59 (1995).